Modelling of Atmosphere Remote Sensing by the Multi-Wavelength LIDAR: Application to Real Signals

Georges DEBIAIS[†,‡], Véronique GUGLIELMI[†], François K. GUEDJE[†,‡]
and Mahouton Norbert HOUNKONNOU[‡]

[†]*ELIAUS, University of Perpignan, 52, Avenue Paul Alduy, F-66860 Perpignan, France*
E-Mail: debiais@univ-perp.fr, veronique.guglielmi@univ-perp.fr

[‡]*International Chair in Mathematical Physics and Applications (ICMPA-UNESCO Chair), University of Abomey–Calavi, 072 B. P. 50, Cotonou, Republic of Benin*
E-Mail: guedjefranco@yahoo.com, norbert.hounkonnou@cipma.uac.bj

LIDAR is one of the cornerstones in the study of the atmosphere. In recent work, we developed a theoretical analysis of the atmosphere response to a monochromatic electromagnetic excitation, as function of altitude, by modelling in a specific way the response of clouds. That analysis established that the density of particles in the cloud can be adequately interpreted in terms of the Lorentzian probability distribution. Theoretical signals thereby generated, fitted with suitable parameters, reproduce the experimental data, making possible a characterisation of the atmosphere with the determination of its significant macroscopic and microscopic physical constants. In the present contribution, that study is refined by considering other relevant distribution laws susceptible to provide a better representation of the particle density as well as an improved model for the LIDAR response. More specifically, we use Rayleigh's law to express the asymmetry sometimes observed in the cloud response. Furthermore, we suggest a theoretical reconstruction of the LIDAR signal which takes into account the influence of the wavelength on the mean free path of photons in the atmosphere.

1 Introduction

Microphysical and optical properties of cloud particles are known to be a great source of information for the understanding of light interactions in the atmospheric system through radiative and chemical processes, hence of the cloud feedback on the Earth's climate. Moreover, clouds are one of the most influential elements in the climatic system, but also one of the most difficult to define. The radiative impact of clouds is double. They reflect a fraction of the incidental solar radiation, thus limiting the part of radiation absorbed by the ground and the oceans. Then, they tend to cool the atmosphere, through the so-called parasol effect. Therefore, they absorb radiation emitted by the Earth and radiate both towards space and back to the ground. Thus, they are involved in the greenhouse effect and contribute to the warming of lower atmosphere layers. All these complex phenomena which contribute to modulate the temperature that we undergo motivate the interest in research activities of the atmospheric system.

In previous work [1,2], we undertook a study of the macroscopic and microscopic physical properties of the atmosphere by using the atmosphere response to a laser excitation generated by a LIDAR. We have proposed a Lorentzian law to model the disturbance and clouds in a LIDAR signal, irrespective of the nature of the atmosphere. Thus, we have inferred a relation involving microscopic parameters of particles such as their size and density. In this contribution, we aim at proposing another model based on probability laws which improve our previous conclusions. New results are given, taking into account simultaneous responses of the atmosphere to various frequencies in the visible electromagnetic spectrum.

2 Overview of the LIDAR Technique

The LIDAR (Light Detection And Ranging) technique is one of the most important optical methods used in the study of the environment. It is a laser based system which technically functions on the same principle as the RADAR (Radio Detection And Ranging), but their ranges of frequencies are clearly different as well as their respective applications. The RADAR uses radio waves from a few meters to a few millimeters, depending on the applications, whereas LIDAR is limited to the electromagnetic waves of the visible spectrum. LIDAR and RADAR are complementary devices often used out in tandem in known scientific satellite observatories such as CALIPSO and CLOUDSAT. For a review of various applications of LIDAR, see Ref. [3]. Figure 1 is a schematic representation of the LIDAR system.

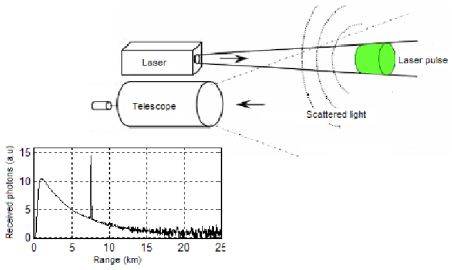

Figure 1. The LIDAR set-up.

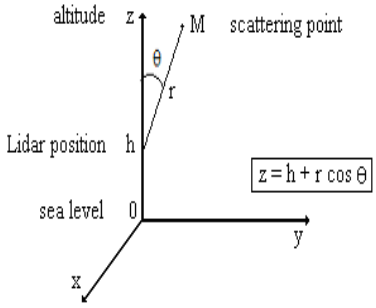

Figure 2. Geometric representation of a LIDAR signal.

2.1 The LIDAR equation

The LIDAR equation expresses the light intensity (more precisely, the power) received back by the telescope after having been scattered by an inhomogeneous medium whose local optical properties depend on the wavelength, λ, and the altitude, z, or distance, r (see Figure 2).

Taking into account the evolution of the solid angle under which the detector is seen from the scattering point and assuming that the scattering is simple, conservative and isotropic, we can express the signal in the following form [2, 4],

$$\ln S(\lambda, h, r) \quad = \quad \ln \frac{1}{4} + \ln \left[\sum_i \alpha_i(\lambda, h, r) \right] - 2 \int_0^r \sum_i \alpha_i(\lambda, h, r)\, dr, \tag{1}$$

with,

$$\alpha(\lambda, h, r) \quad = \quad \sum_i \alpha_i(\lambda, h, r) = \sum_i \frac{1}{\Gamma_i(\lambda, h, r)}, \tag{2}$$

where $\alpha_i(\lambda, h, r)$ is the scattering cross section per unit volume at the scattering point and Γ_i the photon mean free path between two scattering events involving particles of the species i. From this equation, we deduce analytical relations with different laws in order to give a good representation of the mean free path of the photon emitted by the laser in the atmosphere.

2.2 Explicit expression of the excitation wavelength

2.2.1 Classical theory

The particles in the atmosphere and the scattering particles can be studied within the framework of the classical theory of atomic dipolar emission. Consider an electron of mass m and electric charge $-e$, $e > 0$, in the electric field $\vec{E} = \vec{E}_0 e^{-jwt}$ of the excitation electromagnetic wave of the laser. According to the classical model, the electron, in the stationary regime, oscillates around its equilibrium position with the same angular frequency as that of the incident light, and behaves as an oscillating dipole whose moment is $\vec{p} = -e\vec{r}$, $\vec{r}$ being the position vector.

In the electromagnetic theory, the mean power radiated by a dipole is given by,

$$< P >= \frac{1}{4\pi\varepsilon_0}\frac{w^4 p_0^2(w)}{3c^3},$$

$p_0(w)$ being the maximum value of the moment at the frequency w. The dynamics of the electron is described by the second order differential equation,

$$m\frac{d^2z}{dt^2} = -\alpha\frac{dz}{dt} - kz - eE_0e^{-jwt}, \tag{3}$$

where $-\alpha\, dz/dt$ is the force due to viscous friction and $-kz$ is the friction electric force. With $w_0^2 = k/m$, w_0 being the electronic eigenfrequency and $\alpha/m = 1/\gamma$, one obtains,

$$\frac{d^2z}{dt^2} + \frac{1}{\gamma}\frac{dz}{dt} + w_0^2 z = -\frac{e}{m}E_0e^{-jwt},$$

of which the solution in stationary regime is written as,

$$z = \frac{-eE_0e^{-jwt}}{m\left[(w_0^2 - w^2) - j\frac{w}{\gamma}\right]}. \tag{4}$$

It then follows that,

$$p_0^\star(w) = \frac{-e^2E_0}{m\left[(w_0^2 - w^2) - j\frac{w}{\gamma}\right]}, \tag{5}$$

and consequently,

$$< P >= \frac{1}{4\pi\varepsilon_0}\frac{w^4}{3c^3}\frac{e^4E_0^2}{m^2\left[(w_0^2 - w^2)^2 + \frac{w^2}{\gamma^2}\right]}. \tag{6}$$

By introducing the classical electron radius, $R = R_e = e^2/(4\pi\varepsilon_0 mc^2)$, we obtain,

$$< P >= \frac{c\varepsilon_0E_0^2}{2}\sigma(w), \tag{7}$$

with

$$\sigma(w) = \frac{8\pi R^2}{3}\frac{w^4}{\left[(w_0^2 - w^2)^2 + \frac{w^2}{\gamma^2}\right]}, \tag{8}$$

the factor $c\varepsilon_0E_0^2/2$ corresponding to the power per area unit borrowed from the incident electric field; $\sigma(w)$ is the scattering cross section.

The classical theory briefly described above, in spite of its limitation, seems to be sufficient to account for the dependence of the mean scattered power on the angular frequency of the electromagnetic field. Formulated to describe electronic vibrations, this formalism can also be extended to atomic or ionic vibrations, as is the case in spectroscopy. Hence, depending on the value of the atomic radius R or the mass m, one can observe Rayleigh scattering, or resonance Rayleigh scattering, as well as Mie type scattering.

2.2.2 Various types of scattering

The angular eigenfrequency $w_0 = \sqrt{k/m}$ depends on the mass of the scattering element. The electronic eigenfrequency is of the order of $6 \cdot 10^{17}$ rad·s^{-1} while that of a particle or an atmospheric aerosol is estimated to be 10^{14} rad·s^{-1}. These values can be compared with the mean angular frequency of the emitted laser light, $w = 3 \cdot 10^{15}$ rad·s^{-1} corresponding to $\lambda = 500$ nm.

i) For $w \ll w_0$, the Rayleigh scattering condition is realised. Then, the scattering cross section (8) takes the simplified form,

$$\sigma(w) = \frac{8\pi R^2}{3}\left(\frac{w}{w_0}\right)^4. \tag{9}$$

This case corresponds to scattering with electronic vibration and can be used to explain the blue colour of the sky. Light propagates according to such a mechanism in the pure atmosphere.

ii) For $w \cong w_0$, the scattering is called Rayleigh resonance scattering. Then, the scattering cross section can be expressed in the form,

$$\sigma(w) = \frac{8\pi R^2}{3}\frac{w^2}{\left[4(w-w_0)^2 + \frac{1}{\gamma^2}\right]} \cong \frac{8\pi R^2 w_0^2 \gamma^2}{3} L(w), \tag{10}$$

with,

$$L(w) = \frac{1}{1 + 4\gamma^2(w-w_0)^2}.$$

Here, $L(w)$ is a Lorentz frequency function, typical of a resonance. One can thus explain that the red colour of sunset results from a greater scattering than that of the blue colour of sunlight, producing the observation of the remaining red and orange wavelengths.

iii) For $w \mathfrak{g} w_0$, we get Mie type scattering. The particle's mass m becoming large, $1/\gamma$ is negligible and the cross section can be approximated as follows,

$$\sigma(w) \cong \frac{8\pi R^2}{3}, \tag{11}$$

which does not depend on the frequency. Rigorously, Mie theory which involves spherical series, *i.e.*, infinite sums of spherical harmonics, leads, for a spherical particle of radius R and for an incident plane wave, to,

$$\sigma(w) \cong \frac{10\pi R^6}{3}\frac{w^4}{c^4} = \frac{160\pi^5 R^6}{3}\frac{1}{\lambda^4}. \tag{12}$$

If $R \mathfrak{g} \lambda$ (which is nothing but another way of expressing the Mie scattering condition), the wavelength effect is negligible, and the relation (11) remains valid. The white or clear colour of clouds in the sky can be interpreted in this framework. Indeed, the size of cloud droplets being much greater than the visible wavelength, one has Mie type dispersion.

2.2.3 The generalized LIDAR equation

Using the general expression (8) of the cross section $\sigma(w)$ leads to a laser beam angular frequency dependent LIDAR equation. Indeed, the free mean path Γ of photons between two scatterings can be expressed as $\Gamma(z,w) = 1/(n(z)\sigma(w))$, $n(z)$ being the number of atmospheric particles per unit of volume at the altitude z. For particles of species i one can define,

$$\alpha_i(z,w) = \frac{1}{\Gamma_i(z,w)} = \frac{8\pi R^2 n(z)}{3}\frac{w^4}{\left[(w_i^2 - w^2)^2 + \frac{w^2}{\gamma_i^2}\right]}. \tag{13}$$

Let us consider the case when the incident LIDAR laser beam meets, on its path, such "normal" air molecules as the particles of an unspecified disturbance like a cloud. The number of air molecules, $n_a(z)$, per volume unit is well defined by a decreasing exponential law, $n_a(z) = n_{0a}e^{-\chi z}$, where n_{0a} is the density on the ground, close to $2.7 \cdot 10^{19}$ molecules·cm^{-3} and χ is a decreasing constant; $1/\chi$ is about 6 km. These values can vary with the place and the weather conditions. Moreover, Rayleigh's case takes place when the scattering is from molecular origin. One has,

$$\alpha_1(z,w) = \alpha_a(z,w) = \frac{8\pi R_e^2 n_{0a}}{3}e^{-\chi z}\frac{w^4}{w_a^4} = \frac{e^{-\chi z}}{\Gamma_{0a}(w)}\frac{w^4}{w_a^4} = \frac{e^{-\chi z}}{\Gamma_{\mathrm{atm}}(w)}, \tag{14}$$

with

$$\frac{1}{\Gamma_{0a}} = \frac{8\pi R_e^2 n_{0a}}{3}, \qquad \Gamma_{\rm atm}(w) = \Gamma_{0a}(w)\frac{w_a^4}{w^4}.$$

On the contrary, in the case of a disturbance, even when assuming that the particles are identical, their distribution $n_p(z)$ is not known *a priori*. Let us set $n_p(z) = n_0 f(z)$, n_0 being the maximum density, so that the resulting analytical signal may be as much as is possible in agreement with the experimental LIDAR signal. The particles being then larger, the Rayleigh approximation is not longer applicable and we have to take $\alpha_2 = \alpha_p$ such that,

$$\alpha_p(z,w) \quad = \quad \frac{f(z)}{\Gamma_p}\frac{w^4}{\left[(w_p^2 - w^2)^2 + \frac{w^2}{\gamma_p^2}\right]}, \tag{15}$$

with

$$\frac{1}{\Gamma_p} = \frac{8\pi R^2 n_0}{3}.$$

Integrating and taking into account that $z = h + r\cos\theta$, (1) becomes,

$$\begin{aligned}\ln[S(z,w)] \quad = \quad & \ln\left(\frac{1}{4}\right) + \ln\left[\frac{e^{-\chi z}}{\Gamma_{\rm atm}(w)} + \frac{f(z)}{\Gamma_p}\frac{w^4}{[(w_p^2 - w^2)^2 + \frac{w^2}{\gamma_p^2}]}\right] \\ & + \frac{2}{\Gamma_{\rm atm}(w)\chi\cos\theta}[e^{-\chi z} - e^{-\chi h}] \\ & - \frac{2}{\cos\theta}\left[\frac{w^4}{[(w_p^2 - w^2)^2 + \frac{w^2}{\gamma_p^2}]}\frac{1}{\Gamma_p}\int_h^z f(u)\,du\right],\end{aligned} \tag{16}$$

where z stands for the altitude. In the case of multiple disturbances, we have,

$$\begin{aligned}\ln[S(z,w)] \quad = \quad & \ln(\frac{1}{4}) + \ln\left[\frac{e^{-\chi z}}{\Gamma_{\rm atm}(w)} + \sum_i \frac{f_i(z)}{\Gamma_{pi}}\frac{w^4}{[(w_{pi}^2 - w^2)^2 + \frac{w^2}{\gamma_{pi}^2}]}\right] \\ & + \frac{2}{\Gamma_{\rm atm}(w)\chi\cos\theta}[e^{-\chi z} - e^{-\chi h}] \\ & - \frac{2}{\cos\theta}\sum_i\left[\frac{w^4}{[(w_{pi}^2 - w^2)^2 + \frac{w^2}{\gamma_{pi}^2}]}\frac{1}{\Gamma_{pi}}\int_h^z f_i(u)\,du\right].\end{aligned} \tag{17}$$

These new relations which include the angular frequency of the emitted wave are appropriate for the description of the atmosphere response to any frequencies. It is then sufficient to give the particle distribution law, $n(z)$, in the disturbance or cloud, and to integrate as done in our previous work [2] where it was shown that the Lorentz law is very efficient in most cases. However, some experimental signals differ slightly from this law and display an asymmetrical backscattered peak. Hence the necessity to use new laws of probability in order to improve on the results. Given that purpose in mind, we supplement the Lorentzian law by two symmetrical laws, *i.e*, the Gauss and Student laws. For asymmetrical cases, we choose the Rayleigh, Weibull and extreme value laws. The following results concern the case of a standard atmosphere containing only one disturbance (or cloud), in which all the particles are assumed to be identical. In each case, the integral $\int_h^z f(u)/\Gamma_p\,du$ is computed explicitly and then substituted in (16).

In the Figures hereafter, as matter of convenience, illustrations are given with $S(z,w)$ instead of $\ln S(z,w)$, since by doing so it proves to be easier to fit parameters with the experimental signals. Figures are obtained for an average altitude of the cloud equal to $z_0 = 8$ km, which corresponds to a maximum density of the particles, $n_0 = 15$ particles per cubic centimeter, with a density decreasing coefficient of $\tau = 2$ km^{-1}. Moreover, the LIDAR is located at the altitude $h = 1.65$ km and the laser beam is assumed to be vertical, $\theta = 0$.

The other numerical values used are as follows.

- Pure atmosphere: $1/\chi = 6.75$ km, $\Gamma_{\rm atm}(w) = 20$ km for $w = 5 \cdot 10^{15}$ rad·s^{-1} or $\lambda = 350$ nm (violet) with
$$\frac{\Gamma_{\rm atm(\lambda_1)}}{\Gamma_{\rm atm(\lambda_2)}} = \left(\frac{\lambda_1}{\lambda_2}\right)^4 = \left(\frac{w_2}{w_1}\right)^4.$$
- Cloud particles: $R = 1$ μm, $w_p = 2 \cdot 10^{14}$ rad·s^{-1}, $\gamma_p = 10^{-14}$ s, $\Gamma_p = 8$ km at $z = z_0$.

For all the simulated signals, we note that the cloud response corresponding to the red has a greater amplitude than that of the violet. This is explained by the fact that the red frequency is closer to the eigenfrequency of the particle than the violet. It results in that red influences more strongly the particle than any other frequency. On the contrary, the purely molecular response outside the cloud is larger in the violet than at other frequencies since the molecular eigenfrequency is just at the upper limit of the violet frequency range, hence is closer to the violet than the red. The same conclusions are confirmed by the experimental LIDAR signals.

3 Lorentzian (or Cauchy) Law for the Particle Distribution $n(z)$

In this model, the particle density can be expressed as,

$$n(z) = n_0 \, \frac{1}{1 + (z - z_0)^2 \tau^2}, \tag{18}$$

where n_0 is the maximum density of the particles in the cloud corresponding to the altitude z_0, and τ is a constant, parametrising the decrease in the density around z_0. The density behaviour is shown in Figure 3.

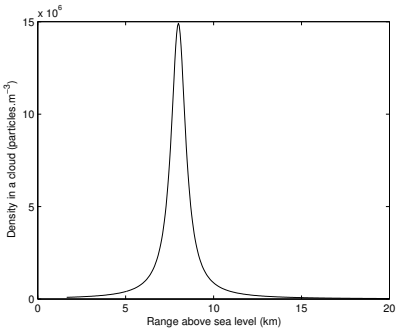

Figure 3: Particle density distribution in a cloud versus the altitude, for a Lorentzian law.

The expression for the integral

$$\int_h^z \frac{f(u)}{\Gamma_p} \, du = \frac{8\pi R^2}{3} \frac{n_0}{\tau} [\tan^{-1}(\tau(z - z_0)) - \tan^{-1}(\tau(h - z_0))], \tag{19}$$

inserted into (16), and taking into account (18), yields the analytical signals $S(z, w)$ illustrated in Figures 4 and 5.

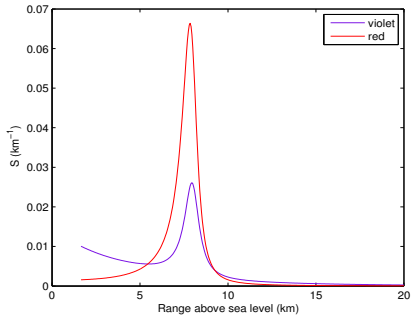

Figure 4. Analytical LIDAR response, $S(z)$, for a Lorentzian law distribution of the particles, at the two wavelengths of 350 and 700 nm.

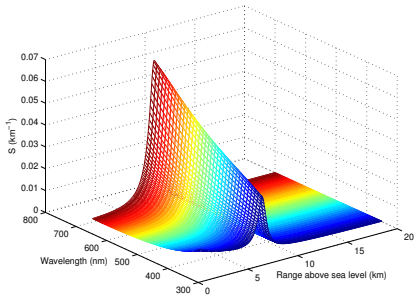

Figure 5. Analytical LIDAR response, $S(z, w)$, for a Lorentzian law distribution of the particles, in the entire visible spectrum.

4 Gauss Law for the Particle Distribution $n(z)$

In the case of the Gaussian law distribution, displayed in Figure 6, the density can be written,

$$n(z) = n_0\, e^{-(z-z_0)^2\tau^2}, \tag{20}$$

and we obtain,

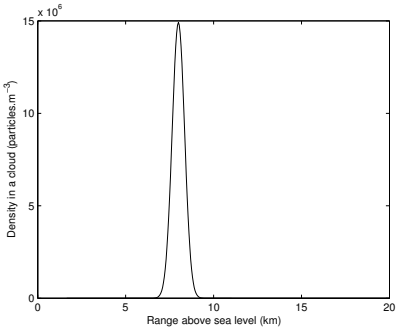

Figure 6: Particle density distribution in a cloud versus the altitude, for a Gaussian law.

$$\int_h^z \frac{f(u)}{\Gamma_p}\, du = \frac{8\pi R^2}{3}\,\frac{\sqrt{\pi}}{2}\,\frac{n_0}{\tau}[erf(\tau(z-z_0)) - erf(\tau(h-z_0))], \tag{21}$$

$erf(x)$ being the error function. Analytical signals are shown in Figures 7 and 8.

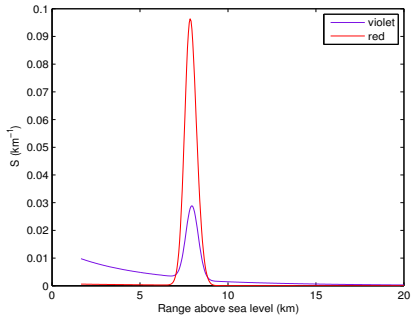

Figure 7. Analytical LIDAR response, $S(z)$, for a Gaussian law distribution of the particles, at the two wavelengths of 350 and 700 nm.

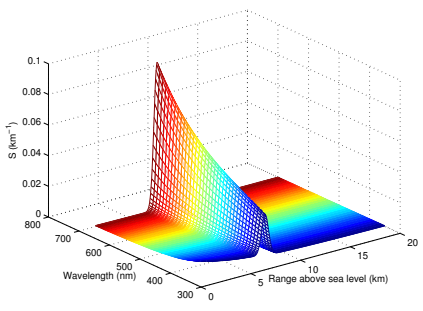

Figure 8. Analytical LIDAR response, $S(z, w)$, for a Gaussian law distribution of the particles, in the entire visible spectrum.

5 Student Law for the Particle Distribution $n(z)$

The case of a Student law distribution corresponds to the relation,

$$n(z) = n_0 \frac{1}{\left[1 + \frac{(z-z_0)^2\tau^2}{\nu}\right]^{\frac{\nu+1}{2}}}, \tag{22}$$

where ν represents the degree of freedom for the Student law distribution, represented in Figure 9.

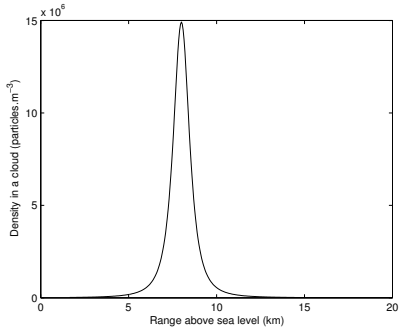

Figure 9: Particle density distribution in a cloud versus the altitude, for the Student law, with $\nu = 2$.

One then obtains,

$$\begin{aligned}\int_h^z \frac{f(u)}{\Gamma_p}\,du &= \frac{8\pi R^2}{3}\frac{n_0}{\tau}\left[(z-z_0)\tau F\left(\frac{1}{2},\frac{\nu+1}{2},\frac{3}{2};-\frac{(z-z_0)^2\tau^2}{\nu}\right)\right.\\ &\left. - (h-z_0)\tau F\left(\frac{1}{2},\frac{\nu+1}{2},\frac{3}{2};-\frac{(h-z_0)^2\tau^2}{\nu}\right)\right],\end{aligned} \tag{23}$$

F being the hypergeometric function defined by,

$$F(a,b,c;x) = \frac{\Gamma(c)}{\Gamma(a)\Gamma(b)}\sum_{k=0}^{+\infty}\frac{\Gamma(a+k)\Gamma(b+k)}{\Gamma(c+k)}\frac{x^k}{k!},$$

while $\Gamma(a)$ is the Euler Gamma function. Figures 10 and 11 illustrate the corresponding analytical signals.

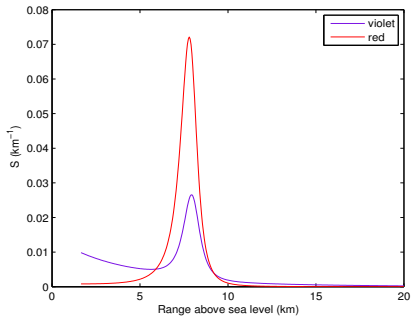

Figure 10. Analytical LIDAR response, $S(z)$, for a Student distribution law of the particles, with $\nu = 2$, at the two wavelengths of 350 and 700 nm.

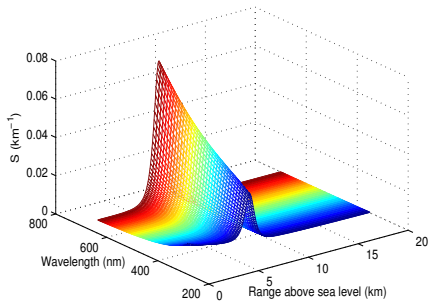

Figure 11. Analytical LIDAR response, $S(z,w)$, for a Student distribution law of the particles, with $\nu = 2$, in the entire visible spectrum.

6 Asymmetric Rayleigh Law for the Particle Distribution $n(z)$

6.1 When the density is larger below than above the cloud center

Using the following model,

$$n(z) = \begin{cases} n_0 \left[1 - (z - z_0)\tau\right] e^{-\frac{1}{2}(z-z_0)^2\tau^2 + (z-z_0)\tau}, & \text{for } z \leq z_0 + \frac{1}{\tau}, \\ 0, & \text{for } z \geq z_0 + \frac{1}{\tau}, \end{cases} \tag{24}$$

corresponding to the distribution represented in Figure 12, one obtains,

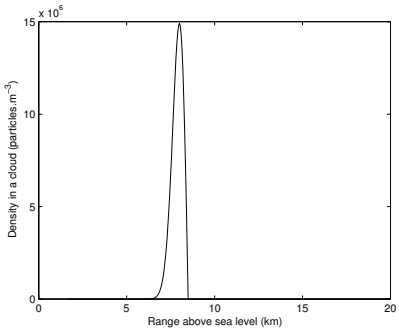

Figure 12: Particle density distribution in an asymmetric cloud bottom versus the altitude, in the case of the Rayleigh law.

$$\int_h^z \frac{f(u)}{\Gamma_p}\, du = \begin{cases} \frac{8\pi R^2}{3}\frac{n_0}{\tau}\left[e^{-\frac{1}{2}(z-z_0)^2\tau^2 + (z-z_0)\tau} - e^{-\frac{1}{2}(h-z_0)^2\tau^2 + (h-z_0)\tau}\right], & \text{for} \quad z \leq z_0 + \frac{1}{\tau}, \\ \frac{8\pi R^2}{3}\frac{n_0}{\tau}\left[e^{\frac{1}{2}} - e^{-\frac{1}{2}(h-z_0)^2\tau^2 + (h-z_0)\tau}\right], & \text{for} \quad z \geq z_0 + \frac{1}{\tau}. \end{cases} \tag{25}$$

The analytical signals are illustrated in Figures 13 and 14.

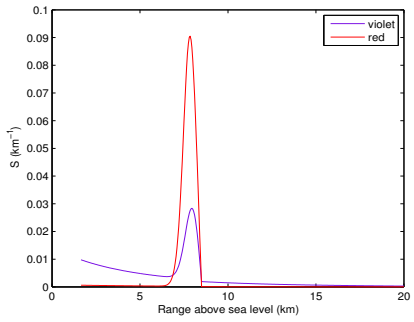

Figure 13. Analytical LIDAR response, $S(z)$, for an asymmetric cloud bottom with the Rayleigh distribution law of the particles, at the two wavelengths of 350 and 700 nm.

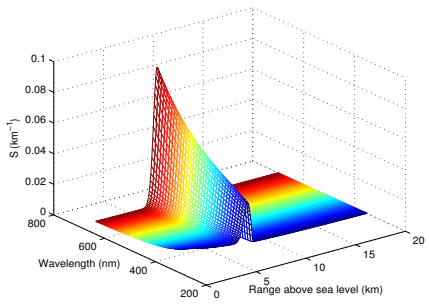

Figure 14. Analytical LIDAR response, $S(z, w)$, for an asymmetric cloud bottom with the Rayleigh distribution law of the particles, in the entire visible spectrum.

6.2 When the density is larger above than below the cloud center

In this case, we have, for a distribution shown in Figure 15,

$$n(z) = \begin{cases} n_0 \left[1 + (z - z_0)\tau\right] e^{-\frac{1}{2}(z-z_0)^2\tau^2 - (z-z_0)\tau}, & \text{for } z \geq z_0 - \frac{1}{\tau}, \\ 0, & \text{for } z \leq z_0 - \frac{1}{\tau}, \end{cases} \tag{26}$$

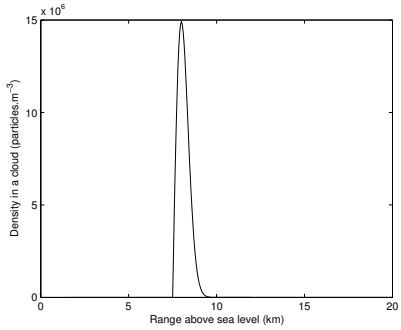

Figure 15: Particle density distribution for the Rayleigh law in an asymmetric cloud top versus the altitude.

One then obtains,

$$\int_h^z \frac{f(u)}{\Gamma_p}\,du = \begin{cases} \frac{8\pi R^2}{3}\frac{n_0}{\tau}[e^{\frac{1}{2}} - e^{-\frac{1}{2}(z-z_0)^2\tau^2-(z-z_0)\tau}], & \text{for } z \geq z_0 - \frac{1}{\tau}, \\ 0, & \text{for } z \leq z_0 - \frac{1}{\tau}. \end{cases} \tag{27}$$

The corresponding analytical signals are illustrated in Figures 16 and 17.

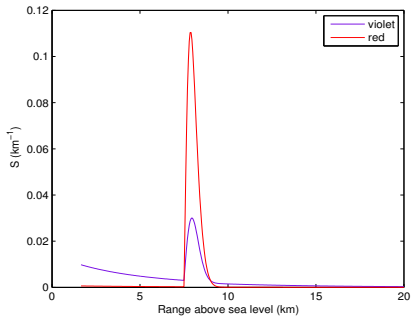

Figure 16. Analytical LIDAR response, $S(z)$, for an asymmetric cloud top with the Rayleigh distribution law of the particles, at the two wavelengths of 350 and 700 nm.

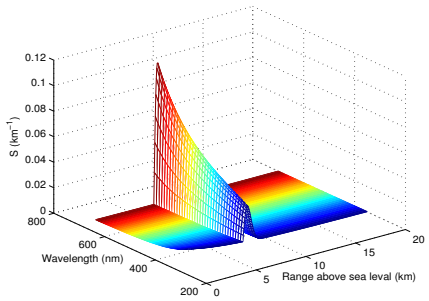

Figure 17. Analytical LIDAR response, $S(z, w)$, for an asymmetric cloud top with the Rayleigh distribution law of the particles, in the entire visible spectrum.

7 Asymmetric Weibull Law for the Particle Distribution $n(z)$

7.1 When the density is larger below than above the cloud center

The coefficient B, introduced hereafter, characterises the shape of the cloud response.

7.1.1 When $1 \leq B \leq 3$

Under this condition we have,

$$n(z) = \begin{cases} n_0 \frac{e^{1-\frac{1}{B}}}{(1-\frac{1}{B})^{1-\frac{1}{B}}}[(1-\frac{1}{B})^{\frac{1}{B}} - (z-z_0)\tau]^{(B-1)}\ e^{-[(1-\frac{1}{B})^{\frac{1}{B}}-(z-z_0)\tau]^B}, & \text{for } z \leq z_0 + \frac{(1-\frac{1}{B})^{\frac{1}{B}}}{\tau}, \\ 0, & \text{for } z \geq z_0 + \frac{(1-\frac{1}{B})^{\frac{1}{B}}}{\tau}. \end{cases} \tag{28}$$

in which case one finds,

$$\int_h^z \frac{f(u)}{\Gamma_p}\,du = \begin{cases} \frac{8\pi R^2}{3}\frac{n_0}{\tau}\frac{e^{1-\frac{1}{B}}}{B(1-\frac{1}{B})^{1-\frac{1}{B}}} \\ \qquad \times[e^{-[(1-\frac{1}{B})^{\frac{1}{B}}-(z-z_0)\tau]^B} - e^{-[(1-\frac{1}{B})^{\frac{1}{B}}-(h-z_0)\tau]^B}], & \text{for } z \le z_0 + \frac{(1-\frac{1}{B})^{\frac{1}{B}}}{\tau}, \\ \frac{8\pi R^2}{3}\frac{n_0}{\tau}\frac{e^{1-\frac{1}{B}}}{B(1-\frac{1}{B})^{1-\frac{1}{B}}}\,[1 - e^{-[(1-\frac{1}{B})^{\frac{1}{B}}-(h-z_0)\tau]^B}], & \text{for } z \ge z_0 + \frac{(1-\frac{1}{B})^{\frac{1}{B}}}{\tau}. \end{cases} \tag{29}$$

7.1.2 When $B \geq 4$

Under this condition we have, as displayed in Figure 18,

$$n(z) = \begin{cases} n_0 \frac{e^{1-\frac{1}{B}}}{(1-\frac{1}{B})^{1-\frac{1}{B}}}[(1-\frac{1}{B})^{\frac{1}{B}} + (z-z_0)\tau]^{(B-1)} \times e^{-[(1-\frac{1}{B})^{\frac{1}{B}}+(z-z_0)\tau]^B}, & \text{for } z \ge z_0 - \frac{(1-\frac{1}{B})^{\frac{1}{B}}}{\tau}, \\ 0, & \text{for } z \le z_0 - \frac{(1-\frac{1}{B})^{\frac{1}{B}}}{\tau}. \end{cases} \tag{30}$$

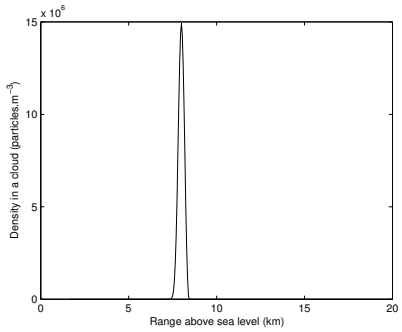

Figure 18: Particle density distribution in an asymmetric cloud bottom versus the altitude, in the case of the Weibull law, with $B = 5$.

One obtains,

$$\int_h^z \frac{f(u)}{\Gamma_p}\,du = \begin{cases} \frac{8\pi R^2}{3}\frac{n_0}{\tau}\frac{e^{1-\frac{1}{B}}}{B(1-\frac{1}{B})^{1-\frac{1}{B}}} \times [1 - e^{-[(1-\frac{1}{B})^{\frac{1}{B}}+(z-z_0)\tau]^B}], & \text{for } z \ge z_0 - \frac{(1-\frac{1}{B})^{\frac{1}{B}}}{\tau} \\ 0, & \text{for } z \ge z_0 - \frac{(1-\frac{1}{B})^{\frac{1}{B}}}{\tau}. \end{cases} \tag{31}$$

The analytical signals are illustrated in Figures 19 and 20.

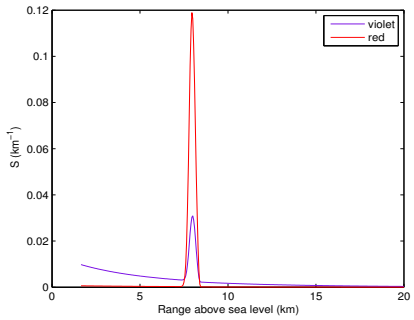

Figure 19. Analytical LIDAR response, $S(z)$, for an asymmetric cloud bottom with the Weibull distribution law of the particles, with $B = 5$, at the two wavelengths of 350 and 700 nm.

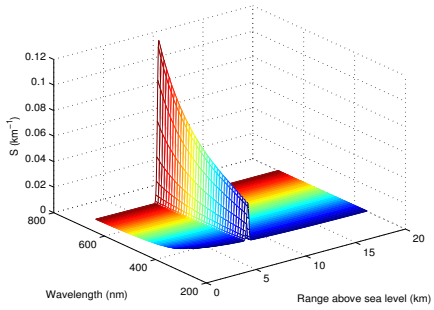

Figure 20. Analytical LIDAR response, $S(z, w)$, for an asymmetric cloud bottom with the Weibull distribution law of the particles, with $B = 5$, in the entire visible spectrum.

7.2 When the density is larger above than below the cloud center

7.2.1 When $1 \leq B \leq 3$

We then have,

$$n(z) = \begin{cases} n_0 \frac{e^{1-\frac{1}{B}}}{(1-\frac{1}{B})^{1-\frac{1}{B}}} [(1-\frac{1}{B})^{\frac{1}{B}} + (z-z_0)\tau]^{(B-1)} \times e^{-[(1-\frac{1}{B})^{\frac{1}{B}} + (z-z_0)\tau]^B}, & \text{for } z \geq z_0 - \frac{(1-\frac{1}{B})^{\frac{1}{B}}}{\tau}, \\ 0, & \text{for } z \leq z_0 - \frac{(1-\frac{1}{B})^{\frac{1}{B}}}{,} \tau \end{cases} \tag{32}$$

and

$$\int_h^z \frac{f(u)}{\Gamma_p}\, du = \begin{cases} \frac{8\pi R^2}{3} \frac{n_0}{\tau} \frac{e^{1-\frac{1}{B}}}{B(1-\frac{1}{B})^{1-\frac{1}{B}}} \times [1 - e^{-[(1-\frac{1}{B})^{\frac{1}{B}} + (z-z_0)\tau]^B}], & \text{for } z \geq z_0 - \frac{(1-\frac{1}{B})^{\frac{1}{B}}}{\tau}, \\ 0, & \text{for } z \leq z_0 - \frac{(1-\frac{1}{B})^{\frac{1}{B}}}{\tau}. \end{cases} \tag{33}$$

7.2.2 When $B \geq 4$

This case corresponds to, as displayed in Figure 21,

$$n(z) = \begin{cases} n_0 \frac{e^{1-\frac{1}{B}}}{(1-\frac{1}{B})^{1-\frac{1}{B}}} [(1-\frac{1}{B})^{\frac{1}{B}} - (z-z_0)\tau]^{(B-1)} \times e^{-[(1-\frac{1}{B})^{\frac{1}{B}} - (z-z_0)\tau]^B}, & \text{for } z \leq z_0 + \frac{(1-\frac{1}{B})^{\frac{1}{B}}}{\tau}, \\ 0, & \text{for } z \geq z_0 + \frac{(1-\frac{1}{B})^{\frac{1}{B}}}{\tau}. \end{cases} \tag{34}$$

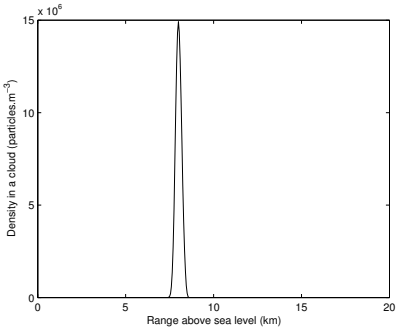

Figure 21: Particle density distribution for the Weibull law in an asymmetric cloud top versus the altitude, with $B = 5$.

One obtains,

$$\int_h^z \frac{f(u)}{\Gamma_p}\, du = \begin{cases} \frac{8\pi R^2}{3} \frac{n_0}{\tau} \frac{e^{1-\frac{1}{B}}}{B(1-\frac{1}{B})^{1-\frac{1}{B}}} \\ \quad \times [e^{-[(1-\frac{1}{B})^{\frac{1}{B}} - (z-z_0)\tau]^B} - e^{-[(1-\frac{1}{B})^{\frac{1}{B}} - (h-z_0)\tau]^B}], & \text{for } z \leq z_0 + \frac{(1-\frac{1}{B})^{\frac{1}{B}}}{\tau}, \\ \frac{8\pi R^2}{3} \frac{n_0}{\tau} \frac{e^{1-\frac{1}{B}}}{B(1-\frac{1}{B})^{1-\frac{1}{B}}} \times [1 - e^{-[(1-\frac{1}{B})^{\frac{1}{B}} - (h-z_0)\tau]^B}], & \text{for } z \geq z_0 + \frac{(1-\frac{1}{B})^{\frac{1}{B}}}{\tau}. \end{cases} \tag{35}$$

The corresponding analytical signals are illustrated in Figures 22 and 23.

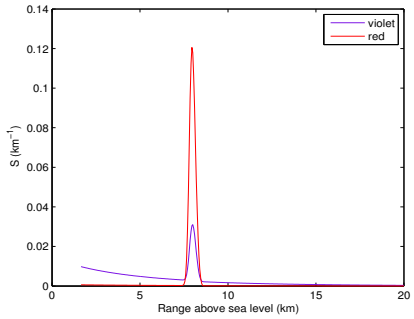

Figure 22. Analytical LIDAR response, $S(z)$, for the Weibull distribution law of the particles, with $B = 5$, in an asymmetric cloud top, at the two wavelengths of 350 and 700 nm.

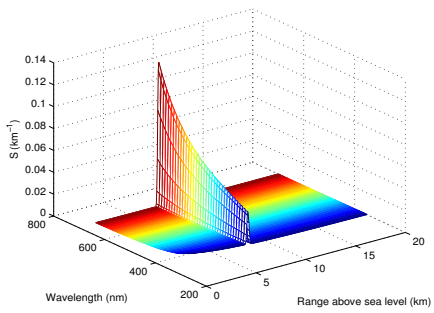

Figure 23. Analytical LIDAR response, $S(z, w)$, for the Weibull distribution law of the particles, with $B = 5$, in an asymmetric cloud top, in the entire visible spectrum.

8 Extreme Value Law for the Particle Distribution $n(z)$

8.1 When the density is larger below than above the cloud center

Given the distribution, illustrated in Figure 24,

$$n(z) \quad = \quad n_0\, e^{1+(z-z_0)\tau} e^{-e^{(z-z_0)\tau}}, \tag{36}$$

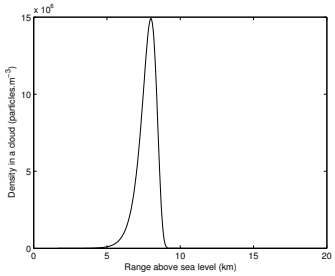

Figure 24: Particle density distribution in an asymmetric cloud bottom versus the altitude, for the extreme value law.

one obtains, as illustrated in Figures 25 and 26 for the corresponding analytical signals,

$$\int_h^z \frac{f(u)}{\Gamma_p}\, du = \frac{8\pi R^2}{3}\frac{n_0}{\tau} e^1 \left[e^{-e^{(h-z_0)\tau}} - e^{-e^{(z-z_0)\tau}} \right]. \tag{37}$$

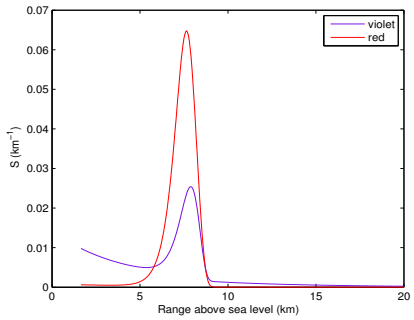

Figure 25. Analytical LIDAR response, $S(z)$, for the extreme value law distribution of the particles, in an asymmetric cloud bottom, at the two wavelengths of 350 and 700 nm.

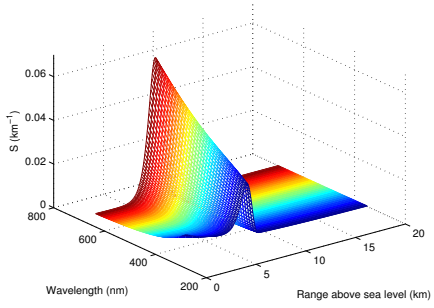

Figure 26. Analytical LIDAR response, $S(z, w)$, for the extreme value law distribution of the particles, in an asymmetric cloud bottom, in the entire visible spectrum.

8.2 When the density is larger above than below the cloud center

Given the distribution, illustrated in Figure 27,

$$n(z) \quad = \quad n_0 e^{1-(z-z_0)\tau} e^{-e^{-(z-z_0)\tau}}, \tag{38}$$

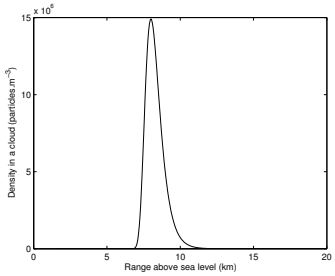

Figure 27: Particle density distribution in an asymmetric cloud top versus the altitude, for the extreme value law.

one obtains,

$$\int_h^z \frac{f(u)}{\Gamma_p}\, du = \frac{8\pi R^2}{3}\frac{n_0}{\tau} e^1 \left[e^{-e^{-(z-z_0)\tau}} - e^{-e^{-(h-z_0)\tau}} \right]. \tag{39}$$

The corresponding analytical signals are illustrated in Figures 28 and 29.

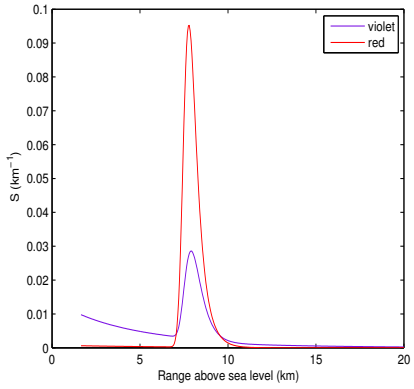

Figure 28. Analytical LIDAR response, $S(z)$, for the extreme value distribution law of particles, in an asymmetric cloud top, at the two wavelengths of 350 and 700 nm.

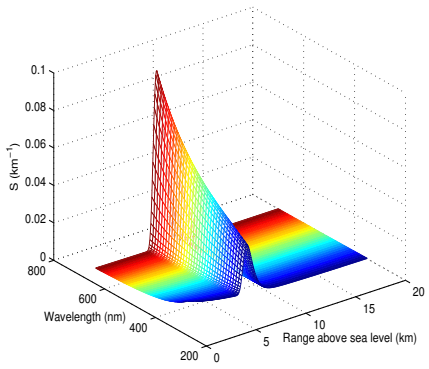

Figure 29. Analytical LIDAR response, $S(z, w)$, for the extreme value distribution law of the particles, in an asymmetric cloud top, in the entire visible spectrum.

9 Application to Real Signals

A significant number of experimental signals obtained at the Thémis site close to Perpignan (France) are available since the research activity of one of the authors (GD) has been in relation to the International CAT and CELESTE Collaborations for the detection of gamma radiation coming from extra-galactic sources [5]. These activities came to an end in 2003. The signals were devoted to identify and quantify the atmosphere quality for gamma ray detection. They correspond to two wavelengths, 355 nm (violet) and 532 nm (green), emitted simultaneously by the laser. Here, in order to test our results and to fit experimental parameters, we consider two typical signals and investigate the particle distribution laws as well as the wavelength influence on the corresponding data. The LIDAR equation established in (17) is used for the analysis.

Although we do not theoretically specify disturbance constraints, we specify the "base" and the "top" of the cloud to correspond to a vanishing slope for the curve fitting the signal. In practice, these base and top define the region of space in which the density of the cloud particles is significant and their difference can represent the cloud thickness. The determination of the mean free path of photons on the ground level is relevant as it gives an idea of the quality of air. Indeed, humid air gives a smaller mean free path than dry air. The dependence of the photon mean free path on the ground level versus the wavelength (in the Rayleigh case) agrees well with the experiments,

$$\frac{\Gamma_{\mathrm{atm}(violet)}}{\Gamma_{\mathrm{atm}(green)}} = \left(\frac{\lambda_{(violet)}}{\lambda_{(green)}}\right)^4.$$

The characteristic decreasing constant, χ, of the molecules in the atmosphere is also in good relation with the air quality. It represents the slope of the linear form of the signal, and its value is sensitive to the humidity or the air pollution. Moreover, the nonlinearity of the curve $\ln S(z)$ reveals the presence of disturbances and clouds in the considered atmosphere.

The constants related to the cloud depend on the altitude, z, and on the time, t (see (3)). We know from the classical theory that $1/\gamma = \beta/m = 2Rw_0^2/(3c)$. Thus, knowing γ and w_0 makes it possible to deduce the particle radius R. Then, by using the relation $1/\Gamma_p = 8\pi R^2 n_0/3$, we deduce the maximum density of the particles as well as their distribution from a given probability law.

The fitted parameters from experimental signals are given for each of the two wavelengths of the laser. The first wavelength, referred to as 01100110, corresponding to a disturbed sky containing three cloud layers, is treated by using the Lorentzian law. See Figures 30 and 31. Table 1 shows the values of the fitted parameters.

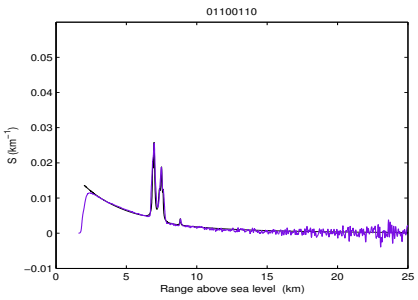

Figure 30. Experimental signal 01100110 (violet), corresponding to a very cloudy atmosphere and analytical signal fitted with the Lorentzian law.

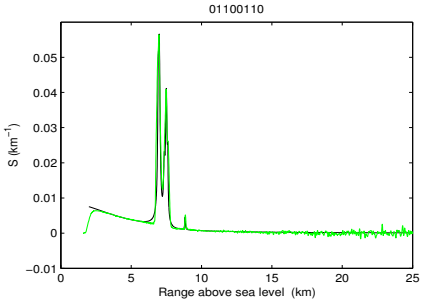

Figure 31. Experimental signal 01100110 (green), corresponding to a very cloudy atmosphere and analytical signal fitted with the Lorentzian law.

The second signal, referred to 05050154, corresponds to a very asymmetric cloud. The signal is analysed with the Rayleigh law. See Figures 32 and 33 and Table 2 for the results.

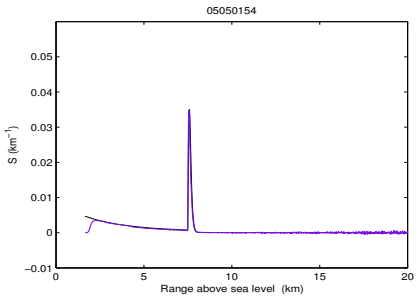

Figure 32. Experimental signal 05050154 (violet), corresponding to a very cloudy atmosphere and analytical signal fitted with the Rayleigh law.

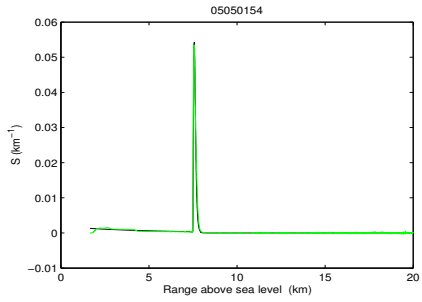

Figure 33. Experimental signal 05050154 (green), corresponding to a very cloudy atmosphere and analytical signal fitted with the Rayleigh law.

Cloud base	$z_{b1} = 6.55$ km, $z_{b2} = 7.31$ km, $z_{b3} = 8.75$ km
Cloud top	$z_{t1} = 7.25$ m, $z_{t2} = 8.25$ km, $z_{t3} = 9.195$ km
Geometric cloud thickness	$e_1 = 0.70$ km, $e_2 = 0.94$ km, $e_3 = 0.45$ km
Photon mean free path on the ground	$\Gamma_{\text{atm}} = 11.8$ km for $\lambda = 355$ nm, and $\Gamma_{\text{atm}} = 59.5$ km for $\lambda = 532$ nm
Characteristic decreasing constant of the molecules in the atmosphere	$\chi = 1/7.2$ km
Particle eigenfrequency	$w_{p1} = 5.0 \cdot 10^{13}$ rad·s^{-1}, $w_{p2} = 4.9 \cdot 10^{13}$ rad·s^{-1}, $w_{p3} = 4.85 \cdot 10^{13}$ rad·s^{-1}
Photon mean free path in clouds	$\Gamma_{p1} = 0.51$ km, $\Gamma_{p2} = 0.89$ km, $\Gamma_{p3} = 3.80$ km
Particle density decreasing constant around the cloud center	$\tau_1 = 16.0$ km^{-1}, $\tau_2 = 17.0$ km^{-1}, $\tau_3 = 22.0$ km^{-1}
Damping coefficient of cloud particles	$\gamma_{p1} = 1.6 \cdot 10^{-13}$ s, $\gamma_{p2} = 1.58 \cdot 10^{-13}$ s, $\gamma_{p3} = 1.57 \cdot 10^{-13}$ s
Particle mean radius	$R_1 = 1.12$ μm, $R_2 = 1.18$ μm, $R_3 = 1.21$ μm
Particle density in center of the cloud	$n_{01} = 186$ particles·cm^{-3}, $n_{02} = 96$ particles·cm^{-3}, $n_{03} = 21$ particles·cm^{-3}

Table 1: Fitted parameters corresponding to the experimental signal 01100110 (violet and green) treated with the Lorentzian law.

Cloud base	$z_b = 7.48$ km
Cloud top	$z_t = 8.13$ km
Geometric cloud thickness	$e = 0.650$ km
Photon mean free path on the ground	$\Gamma_{\text{atm}} = 11.6$ km for $\lambda = 355$ nm, and $\Gamma_{\text{atm}} = 58.7$ km for $\lambda = 532$ nm
Characteristic decreasing constant of the molecules in the atmosphere	$\chi = 1/7.0$ km
Particle eigenfrequency	$w_p = 1.0 \cdot 10^{13}$ rad·s^{-1}
Photon mean free path in cloud	$\Gamma_p = 0.0052$ km
Particle density decreasing constant around the cloud center	$\tau = 8.4$ km^{-1}
Damping coefficient of cloud particles	$\gamma_p = 3 \cdot 10^{-13}$ s
Particle mean radius	$R = 15$ μm
Particle density in center of the cloud	$n_0 = 102$ particles·cm^{-3}

Table 2: Fitted parameters corresponding to the experimental signal 05050154 (violet and green) treated with the Rayleigh law.

10 Concluding Remarks

The obtained results are in good agreement with data known in the literature [6]. The distance dependent parameters are given with a satisfactory accuracy (about 6%). The frequency dependence has been difficult to simulate as the cloud particles are relatively large, thus giving rise to a scattering close to one of the Mie type. Indeed, the computed cross section does not vary too much with the frequency and the fitting of the corresponding parameters is difficult to perform; the green signal gives the best evaluation. The accuracy on the parameter determination is estimated to be 15%; it is about 20% for particle radius and density determinations. These results, far from being only qualitative, are relevant for the analysis of real data.

For the signal 01100110, we have determined the particle mean radii in three successive clouds. Apparently, these radii slightly increase with altitude. On the contrary, the mean density of the particles in each cloud center clearly decreases with altitude, a conclusion which is consistent with the height of the signal peaks.

The cloud signal 05050154 is composed of the largest particles, practically with a radius ten times greater than the preceding cloud radii, and with a higher density. These results explain the extremely intense reflection peak that is observed.

On the whole, we have obtained by this method of processing the LIDAR signal detailed information on the atmosphere parameters. This method of the particle radii and density determination by remote sensing is new. However, it is useful to emphasize that this entire study is performed under the assumption that particles are identical and spherical. Such a condition is not realistic for the scattering in clouds containing different species of particles like aerosols, microscopic water drops or crystallites of ice. As suggested in Ref. [7], the distribution of the particle radii in a cloud could also be analysed within the framework of a formalism based on probability laws similar to those used here for the particle density evolution. Such an investigation will be addressed in a forthcoming paper.

References

[1] G. Debiais and M. N. Hounkonnou, *Optical Parameter Determination of the Atmosphere from a LIDAR Signal by Hilbert Transforms. Attempt at Aerosol Characterization*, in the *Proceedings of the Third International Workshop on Contemporary Problems in Mathematical Physics*, eds. J. Govaerts, M. N. Hounkonnou and A. Z. Msezane (World Scientific, Singapore, 2004), pp. 188–208.

[2] G. Debiais, F. K. Guedje and M. N. Hounkonnou, *A New Analytical Approach to the Atmosphere Characterization by a Backscattered LIDAR Signal*, in the *Proceedings of the Fourth International Workshop on Contemporary Problems in Mathematical Physics*, eds. J. Govaerts, M. N. Hounkonnou and A. Z. Msezane (World Scientific, Singapore, 2006), pp. 212–229.

[3] P. H. Flamant, *Atmospheric and Meteorological LIDAR: From Pioneers to Space Applications*, *C. R. Physique* **6**, 864–875 (2005).

[4] A. Saka, *Model of Atmospheric Scattering. Theory of LIAR*, Ph.D. Thesis (University of Perpignan, France, 1998), unpublished.

[5] CELESTE Collaboration, *An Atmospheric Cherenkov Telescope for High Energy Gamma Ray Astrophysics*, *Nuclear Instrument and Method A* **490**, 79–89 (2002).

[6] L. W. Carrier, G. A. Cato and K. J. Von Essen, *The Backscattering and Extinction of Visible and Infrared Radiation by Selected Major Cloud Models*, *Applied Optics* **6**, 1209–1216 (1967).

[7] D. Deirmendjian, *Electromagnetic Scattering on Spherical Polydispersions* (American Elsevier, New York, 1969).